ACS NANOSCIENCE Au
AN OPEN ACCESS JOURNAL OF THE AMERICAN CHEMICAL SOCIETY

pubs.acs.org/nanoau
Article

Controlling Morphology and Excitonic Disorder in Monolayer WSe_2 Grown by Salt-Assisted CVD Methods

Reynolds Dziobek-Garrett, Sachi Hilliard, Shreya Sriramineni, Ona Ambrozaite, Yifei Zhu, Bethany M. Hudak, Todd H. Brintlinger, Tomojit Chowdhury, and Thomas J. Kempa*

Cite This: ACS Nanosci. Au 2023, 3, 441–450
Read Online

ACCESS | Metrics & More | Article Recommendations | Supporting Information

ABSTRACT: Chemical synthesis is a compelling alternative to top-down fabrication for controlling the size, shape, and composition of two-dimensional (2D) crystals. Precision tuning of the 2D crystal structure has broad implications for the discovery of new phenomena and the reliable implementation of these materials in optoelectronic, photovoltaic, and quantum devices. However, precise and predictable manipulation of the edge structure in 2D crystals through gas-phase synthesis is still a formidable challenge. Here, we demonstrate a salt-assisted low-pressure chemical vapor deposition method that enables tuning W metal flux during growth of 2D WSe_2 monolayers and, thereby, direct control of their edge structure and optical properties. The degree of structural disorder in 2D WSe_2 is a direct function of the W metal flux, which is controlled by adjusting the mass ratio of WO_3 to NaCl. This edge disorder then couples to excitonic disorder, which manifests as broadened and spatially varying emission profiles. Our work links synthetic parameters with analyses of material morphology and optical properties to provide a unified understanding of intrinsic limits and opportunities in synthetic 2D materials.

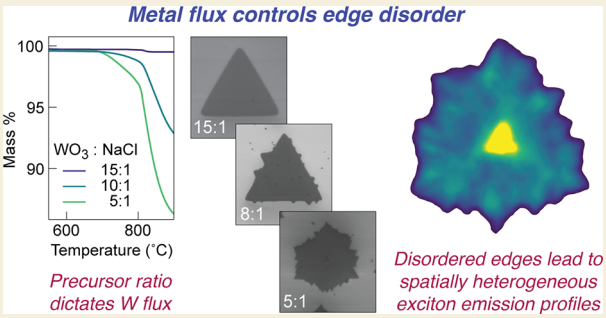

KEYWORDS: *2D materials, transition-metal dichalcogenide, chemical vapor deposition, crystal morphology, crystal defects, exciton, photoluminescence*

INTRODUCTION

Monolayer transition metal dichalcogenides (TMDs) are an attractive materials platform for optoelectronic,[1−3] nano-electronic,[4,5] and quantum device studies.[6−8] Notably, TMD crystals are excellent candidates for exploring light−matter interactions at the 2D limit[9] because they exhibit a direct bandgap in monolayer form,[10] a strong coupling of optical stimulation to excitonic states,[11] and spin−valley coupling.[12] While monolayers exfoliated from bulk crystals are commonly used for proof-of-concept devices and spectroscopic experiments, exfoliation frequently results in strained or torn crystals and rarely yields sample sizes greater than 100 μm.[13] Direct bottom-up synthetic techniques involving chemical vapor deposition (CVD) offer a promising route toward scalable production of intact and larger area monolayer TMD crystals, which is vital to realization of these materials' transformative potential in science and technology.[14] In particular, recent breakthroughs in CVD growth of TMD monolayers have enabled researchers to precisely tune crystal properties through morphology and phase engineering.[15−17]

The reliability and impact of these synthetic methods are defined by the extent to which the relationship between synthetic parameters and resulting material properties is understood. The presence of grain boundaries, intrinsic strain, and lattice defects in the synthesized samples remains an outstanding challenge. These imperfections have immense consequences for the properties of monolayer TMDs[18−20] and often render them of insufficiently high quality to supplant exfoliated crystals in champion device studies.[21] Strain often arises in synthesized 2D TMDs either due to thermal mismatch between the crystal and its growth substrate or due to bending of the crystal over rough substrates.[22,23] Moreover, ordered vacancies or defects, which can act as scattering sites for excitons and charge carriers, are often located at grain boundaries formed when multiple growing crystals intersect.[18,19] Finally, while synthetic monolayers can express unfragmented native crystal edges that express catalytically or electronically active atomic terminations,[24] imbalanced precursor fluxes during growth can alter the edge structure leading to excess free carriers which enhance trion and biexciton emission.[25,26] The termination of crystal edges or boundaries also offers tantalizing prospects for designing nontrivial states which differ from the bulk such as gap-states,[27]

Received: June 19, 2023
Revised: August 8, 2023
Accepted: August 8, 2023
Published: August 22, 2023

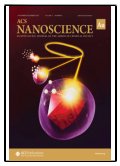

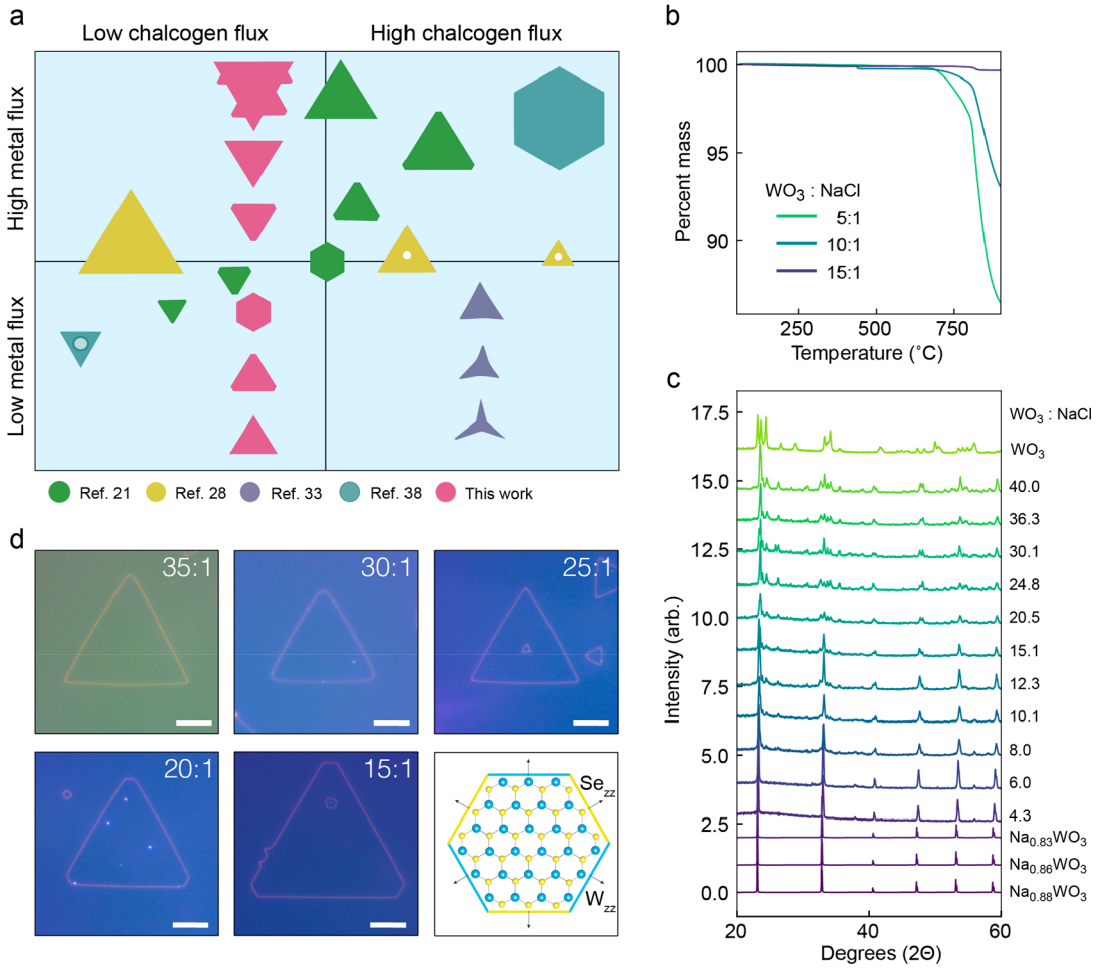

Figure 1. (a) Summary of the 2D TMD crystal synthesis parameter space explored by other researchers and their observed crystal morphologies. The relative position of each crystal schematic within a referenced data set is an accurate estimate of the parameter space within which that crystal was prepared. The scheme diagonal represents a 1:2 M:X ratio. With the exception of this work (red), each reference study was conducted on MoS_2. (b) Thermogravimetric analysis (TGA) data collected on W precursor samples prepared at WO_3:NaCl ratios of 5:1, 10:1, and 15:1. The first minimal mass loss event at ∼400 °C can be attributed to a minor impurity that is inconsequential to the reaction. (c) Powder X-ray diffraction (pXRD) data collected on W precursors prepared across a range of WO_3:NaCl ratios. Also included are calculated pXRD scans of Na_xWO_3 bronzes from ref 40. (d) Dark-field optical images of WSe_2 crystals grown at high WO_3:NaCl ratios. Schematic: Competition in the rate of growth of W_{zz} and Se_{zz} edges defines the range of 2D WSe_2 crystal shapes and facet terminations. Scale-bars: 10 μm.

metallic[28] or ferromagnetic[29] edges, and topological states at grain boundaries,[30] all of which have been observed in WSe_2. Since strain, lattice defects, and edge inhomogeneities hamper device performance, synthetic strategies addressing these sources of disorder are urgently needed.

Precursor flux at the crystal growth front is a critical determinant of the morphology, defect density, and edge termination of TMD crystals.[31−33] The relative fluxes of transition metal (M) and chalcogen (X) precursors define a diverse array of TMD crystal shapes and sizes (Figure 1a). For example, if there is relative parity in the flux of M and X precursors, then one expects roughly equivalent growth rates for the thermodynamically stable M-terminated or X-terminated zigzag edges (M_{zz} and X_{zz}), which lead to hexagon- or triangle-shaped TMD crystals.[34] Much of this parameter space has been studied extensively for the case of Mo-based TMDs.[35−38]

A major reason for the shortfall in synthetic studies examining W-based TMDs is the difficulty in evaporating WO_3, the most common precursor for WX_2 crystals.[39] One strategy to circumvent this challenge is to mix alkali metal halide salts with WO_3 to form a more volatile precursor[40,41] which can be used in CVD growth of WS_2 and WSe_2 crystals. While this strategy has been shown to yield triangle-shaped and hexagon-shaped WX_2 crystals, studies reporting crystals with unusual morphologies[40,41] and serrated edges have not commented on the chemical origin of these growth features.

Here, we show that precise tuning of the volatility of the W precursor through adjustment of the WO_3 to NaCl ratio allows systematic control of TMD (in this case WSe_2) crystal morphology. We also examine the dependence of the crystal emission properties on morphology and local defects through photoluminescence mapping. Our results not only provide much-needed insights regarding morphology control of W-based TMDs, which have received much less attention, but also establish a rigorous connection between synthetic parameters and their influence on TMD optical properties.

RESULTS AND DISCUSSION

We first examined the structure and volatility of mixtures of WO_3 and NaCl. For all syntheses we discuss below, the NaCl amount is fixed, and WO_3 is varied to alter the precursor ratio.

https://doi.org/10.1021/acsnanoscienceau.3c00028
ACS Nanosci. Au 2023, 3, 441−450

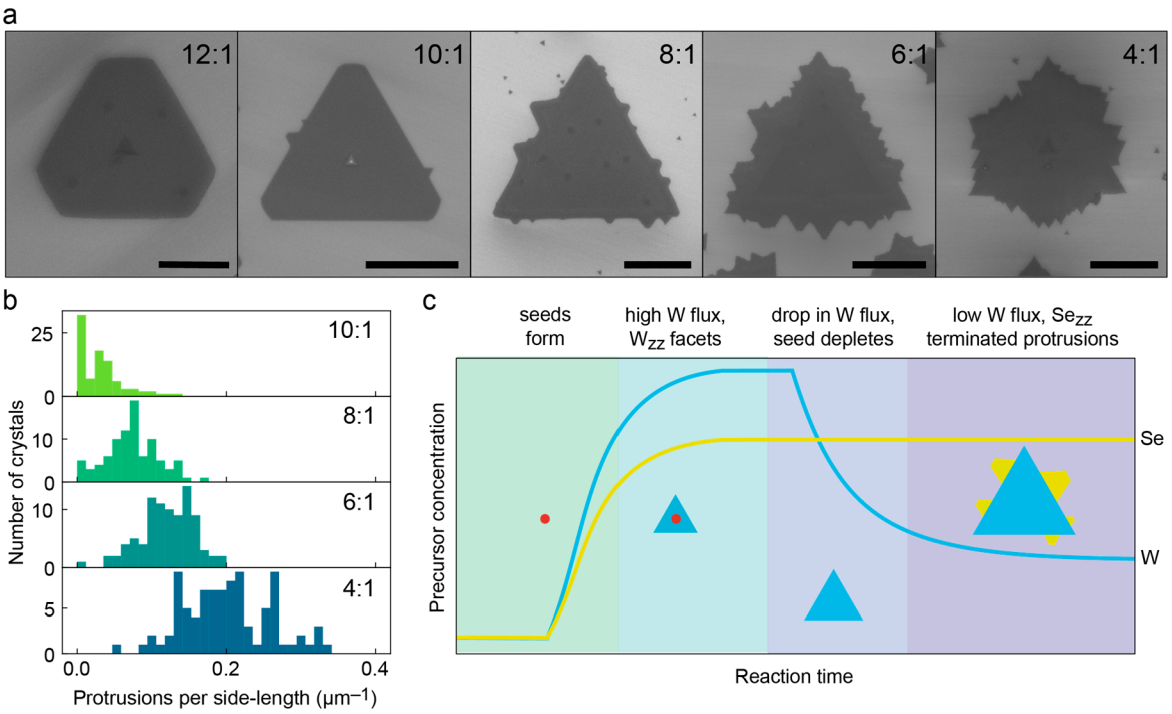

Figure 2. (a) SEM images of WSe_2 crystals grown from W precursors prepared at different WO_3:NaCl ratios. The images are listed in order of increasing W volatility (decreasing the WO_3:NaCl ratio). Scale-bars: 5 μm (12:1), 20 μm (10:1, 8:1, 6:1), 10 μm (4:1). (b) Histograms of the number of protrusions per μm of crystal edge length as surveyed from wide-field SEM images collected on samples prepared at each ratio indicated in the top right. (c) Schematic proposal of the growth mechanism for 2D crystals with jagged edges. A seed (pink dot) is formed first and is composed of the tungsten oxychloride deposit, which steadily alloys with the steady-state flux of Se (yellow line). Following this, WSe_2 grows in an environment of high W flux (blue line), yielding a 2D crystal with W_{zz}-terminated facets. As the reaction progresses, the W flux drops relative to the Se flux as the seed becomes steadily depleted of W. This imbalance results in accelerated growth of W_{zz} edges and concomitant expression of Se_{zz}-terminated protrusions.

Low ratios of WO_3:NaCl exhibit onset of mass loss at lower temperatures than pure WO_3 as determined by thermogravimetric analysis (TGA). Specifically, samples containing a WO_3:NaCl ratio of 5:1 (the lowest we tested by TGA) lose nearly 10% of their mass before the highest ratio of 15:1 loses 1% of its mass (Figure 1b). Powder X-ray diffraction (pXRD) scans of samples composed of a range of annealed mixtures of WO_3 and NaCl reveal several details (Figure 1c). A triplet of peaks at $2\theta = 22°$ and a series of broadened peaks at $2\theta = 33°$ merge into single peaks at $2\theta = 23.4°$ and $2\theta = 33.25°$ in samples containing WO_3:NaCl ratios below 20:1. Reflections in the WO_3 diffraction pattern are consistent with the calculated pattern for triclinic WO_3,[42] which shows three prominent peaks around $2\theta = 22°$ from the (200), (020), and (002) planes and collections of weaker peaks at higher angles which merge into broadened peaks in the experimental diffraction pattern (Figure S1). In diffraction patterns collected from annealed WO_3:NaCl mixtures, the two most prominent peaks around $2\theta = 23°$ and $2\theta = 33°$ associated with the 15:1 sample agree well with reflections from the (100) and (110) planes observed in Na_xWO_3 bronzes studied by Straumanis.[43] Moreover, we observe peak shifts to lower 2θ as the WO_3:NaCl ratio decreases, and this trend is consistent with incorporation of higher Na concentrations in these mixtures.[43] These data provide evidence for the formation of a new, more volatile, crystalline phase upon increasing incorporation of Na (lower WO_3:NaCl ratios) and suggest that $Na_xWO_{(3-x)}Cl_x$ is the volatile W precursor species formed during salt-assisted CVD growth of W-based TMDs. An alloy of this form has been postulated, without compelling experimental evidence, to be the intermediate in salt-assisted TMD reactions.[44] These experiments establish a strategy for tuning the W flux through control of W precursor volatility.

To examine how crystal morphology evolves with W flux, we conducted WSe_2 syntheses across a range of WO_3:NaCl ratios. For every reaction discussed below, the degree (low or high) of the W flux is considered relative to the Se flux, with the latter being held constant across all syntheses. We first examined reactions conducted at "low" W flux, which we associate with WO_3:NaCl ratios higher than 15:1. Crystals evolve from well-defined triangular shapes at ratios of 35:1 (lower W flux) to triangular shapes with flattened corners at ratios of 15:1 (higher W flux), as seen in dark-field optical images (Figure 1d). The triangle-shaped crystals likely have Se_{zz}-terminated facets, since the growth rate of W_{zz} edges exceeds that of Se_{zz} edges when the W flux is relatively lower than that of Se. Kinetic Monte Carlo calculations predict faster $metal_{zz}$ over $chalcogen_{zz}$ facet growth and attribute this to preferential metal adsorption on $metal_{zz}$ edges saturated with under-coordinated chalcogen atoms, which is to be expected under our conditions of excess chalcogen flux.[38] The onset of flattened corners in the crystals can be associated with W_{zz}-terminated facets that begin to appear as the growth rate of Se_{zz} edges becomes competitive with that of W_{zz} edges when the W flux approaches that of Se. This competition between facet growth rates determines the ultimate crystal shape and is summarized in the schematic of Figure 1d. Our observations of growth within the "low flux" regime are consistent with reports tracing the evolution of crystal shape as reaction conditions shift from substantial chalcogen excess to W:Se ratios of 1:2.[34,38]

https://doi.org/10.1021/acsnanoscienceau.3c00028
ACS Nanosci. Au 2023, 3, 441−450

We next examined WSe_2 crystal growths conducted at "high" W flux conditions (WO_3:NaCl ratios less than 15:1). A WO_3:NaCl ratio of 12:1 yields nearly hexagonal crystals, in accordance with the trend discussed above (Figure 2a). This observation suggests roughly equivalent growth rates for W_{zz}- and Se_{zz}-terminated facets as the W flux and Se flux reach parity. One would predict that further increasing the W flux through lower WO_3:NaCl ratios should increase the growth rate of the Se_{zz} edges such that the crystal assumes a triangle shape with W_{zz}-terminated facets.

However, as the W flux is increased by using WO_3:NaCl ratios less than 10:1, we observe the onset of anomalous crystal growth modes. Notably, for ratios less than 10:1, SEM images reveal that protrusions begin to grow from the crystal edges (Figure 2a). The density of these protrusions per unit edge length increases sharply as the WO_3:NaCl ratio decreases below 8:1 (Figure 2b) until the crystals exhibit a fractal-like edge morphology. Low-magnification SEM and optical images (Figures S2, S3) and statistical analyses (Figure 2b) confirm that these trends persist over many sampled crystals. These jagged edges are similar to those reported by other groups for the case of WX_2 crystals grown with alkali metal halide promoters.[40,41] A closer analysis suggests that the protrusions are terminated by Se_{zz} facets, which are opposite to the W_{zz} facets expressed by the "parent" crystal from whence the protrusions nucleated (Figure S4). As stated above, we expect that high W fluxes should yield crystals with W_{zz}-terminated facets due to rapid Se_{zz} edge growth. The observation that the protrusions exhibit mirror symmetry (Figure S4) about the edge axis further supports the expectation that the protrusions are Se_{zz}-terminated.

The WSe_2 crystal morphology can serve as a reporter on the relative growth rates of the Se_{zz} and W_{zz} edges and can be used to construct a timeline and mechanism for the anomalous growth observed during synthesis at low WO_3:NaCl ratios (Figure 2c). High-resolution SEM images of reactions run for 1 min, as compared to 3 min for the full reaction, contain incipient crystals with large seeds at their center (Figure S5). These data suggest a *first stage* of growth (Figure 2c, purple region) that involves an induction period during which the volatile tungsten oxychloride species deposited on the Si/SiO_2 substrate form alloys with Se[32,45−47] and seed the WSe_2 crystal growth. Moreover, analysis of a sample prepared at a 6:1 WO_3:NaCl ratio reveals predominantly jagged-edged crystals and some straight-edged triangular crystals which have average edge lengths of 41.7 ± 0.9 μm and 15.1 ± 0.6 μm, respectively (Figure S6). The smaller straight-edged crystals are likely the result of reaction that progressed through the end of a *second stage* of growth (Figure 2c, violet/blue region) that can be associated with a high flux of W to the crystal growth front from the W-rich seed at early times. These straight-edged triangular crystals most likely possess W_{zz}-terminated facets, given that high relative W flux yields faster Se_{zz} edge growth. The larger jagged-edged crystals point to a *third stage* of growth (Figure 2c, green region), during which uneven facet growth takes place. We attribute the nucleation and growth of the protrusions to reduction of W flux relative to Se flux at the crystal edge, as the tungsten oxychloride seed is depleted of W. This is expected to lead to accelerated growth of W_{zz} edges with concomitant expression of Se_{zz}-terminated facets. At longer times, as the seed becomes more fully depleted, the imbalance between the growth rates of Se_{zz} edges and W_{zz} edges increases further and leaves many parts of the W_{zz} edges terminated by under-coordinated Se. These latter edges are thermodynamically unstable and serve as nucleation sites for growth of the protrusions, which rapidly become terminated by Se_{zz} facets due to excess Se. The stochastic pattern of the protrusions may be due to the inhomogeneous distribution of the W precursor along the crystal growth front or the presence of random defects that serve as nucleation centers.

We tested this hypothesis by conducting timed reactions at 1 min intervals and characterizing the crystal products by SEM (Figure S5). For reactions run for 1 min at the growth temperature, we observe crystals with highly disordered growth fronts and prominent seeds at their center. After 2 min, the monolayer crystal coalesces into its expected triangular shape with a large central seed still present. After 3 min, the seed size is significantly reduced and jagged edges begin to emerge. We note that these experiments were conducted at a lower temperature in order to slow the reaction kinetics and thereby allow for temporal resolution of the crystal growth progress.

To provide additional evidence for our proposed mechanism and related edge assignments, we conducted aberration-corrected high-angle annular dark field scanning transmission electron microscopy (HAADF-STEM) at the intersection of a WSe_2 crystal with one of its edge protrusions (Figure 3a, Figure S7). High-resolution and Fourier-filtered HAADF-STEM images and corresponding pixel contrast variations viewed along the arm-chair direction of the lattice within both the "parent" crystal and the protrusion reveal the same crystal orientation and expected 2H phase throughout these two regions (Figure 3b,d,e,g). We assign the brighter atoms as W and darker atoms as Se due to the larger expected scattering cross-section of W compared to two stacked Se atoms. By superimposing the WSe_2 structure on a lattice-resolved image of the crystal, we can clearly identify the orientation of the lattice and index all directions and planes (Figure 3c,f). Using these data as a reference point, we can assign the protrusion (region "d" in Figure 3a) to Se-terminated zigzag edges and the parent crystal (regions "b" and "e" in Figure 3a) to W-terminated zigzag edges. While we cannot rule out the possibility that some edge protrusions arise due to mirror-twin boundaries, possibly arising due to the dramatic change of precursor flux, our HAADF-STEM data do not reveal the presence of such boundaries. In short, our results support the conclusion that the WSe_2 crystal lattice orientation is preserved across the parent crystal and its protrusions and that the edges of the protrusion are Se_{zz}.

To identify any structural or topographical anomalies associated with crystals grown for WO_3:NaCl ratios below 10:1, we collected Raman maps and atomic force microscopy (AFM) scans. Raman maps imaging the characteristic E′ mode of WSe_2 (250 cm^{-1}) reveal that the intensity of this mode is uniform across each crystal for every synthesis condition (10:1, 8:1, 6:1, and 4:1 ratios), with no noticeable intensity anomalies near the crystal edges (Figure 4a−d). Point and line spectra taken for crystals prepared at each of the aforementioned synthesis conditions reveal exceptionally uniform Raman responses (Figure 4e, Figure S8). AFM maps reveal that the crystals are of uniform height and, with the exception of isolated regions of bilayer growth, are largely monolayers with heights of 1 nm (Figure 4f−i). High-resolution AFM maps and line scans show no evidence of grain boundaries or height anomalies at the junctions between protrusions and their parent crystal (Figure 4j, Figure S9). The foregoing Raman and AFM data suggest that the crystals are continuous and

https://doi.org/10.1021/acsnanoscienceau.3c00028
ACS Nanosci. Au 2023, 3, 441−450

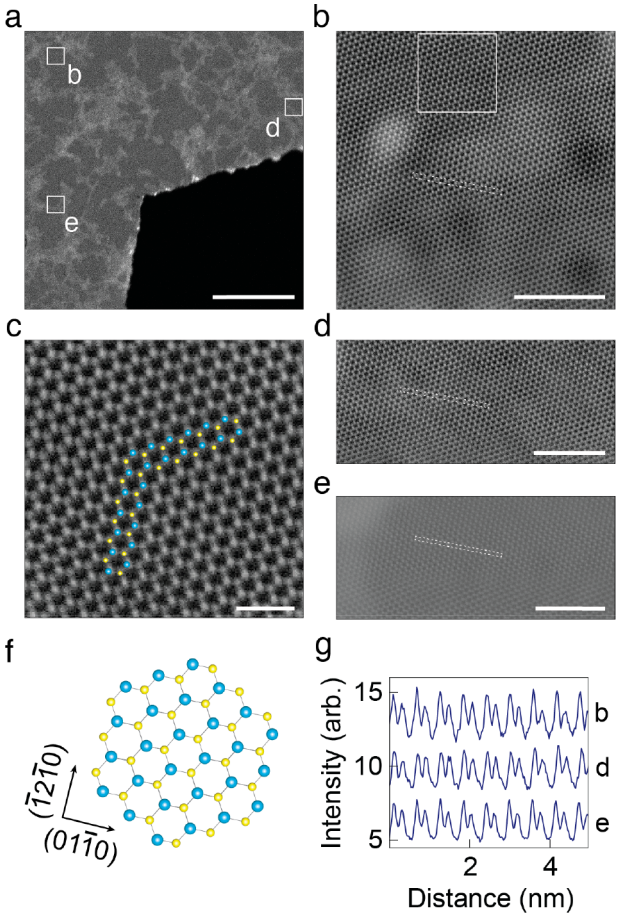

Figure 3. (a) HAADF-STEM image of the intersection between a parent 2D WSe_2 crystal and one of its protrusions. The TEM sample was prepared by transferring a crystal to a perforated silicon nitride membrane. Regions "b" and "e" are within the parent crystal, and region "d" is within the protrusion. Scalebar: 50 nm. (b) High-resolution, Fourier-filtered HAADF-STEM image from the white-boxed region labeled "b" in (a). Scalebar: 4 nm. (c) Zoomed-in image of the white-boxed region in (b) with a cartoon of the WSe_2 crystal structure superimposed. Blue spheres represent W atoms, and yellow spheres represent Se. Scalebar: 1 nm. (d) High-resolution, Fourier-filtered HAADF-STEM image from the white-boxed region labeled "d" in (a) Scalebar: 4 nm. (e) High-resolution, Fourier-filtered HAADF-STEM image from the white-boxed region labeled "e" in (a). Scalebar: 4 nm. (f) Schematic of the WSe_2 crystal structure with armchair and zigzag planes indexed. (g) Plots of pixel count intensity for line scans taken along the armchair direction of the crystal lattice from the rectangular regions marked by dashed boxes in (b), (d), and (e).

homogeneous, and there is no evidence to suggest that the jagged edges are the result of triangular intergrowths.

Having identified through Raman and AFM mapping that the crystals appear to be structurally homogeneous, we assessed their photoemission properties through far-field photoluminescence (PL) measurements. An analysis of PL spectra collected at various points within a triangle-shaped crystal with mostly straight edges (WO_3:NaCl ratio 10:1) reveals emission that varies significantly in intensity across the crystal but exhibits minor variation in peak wavelength or peak width (Figure S10). However, a similar point analysis of a crystal grown under higher W flux (WO_3:NaCl ratio of 4:1) reveals not only variable and weaker emission intensity, but also a larger spread in peak wavelength and peak width compared to the straight-edge crystal (Figure S10). The emission centered at 778−780 nm, which we observe in the 10:1 crystal sample, is consistent with previous reports of exciton emission from grown and exfoliated 2D WSe_2 flakes.[20]

For a more detailed assessment of any spatial variation in the emission properties of the WSe_2 crystals, we obtained hyperspectral PL data. 2D TMD crystals exhibit strong coupling of light to excitonic states, which are themselves highly sensitive to local dielectric environment and other crystallographic features.[11] PL maps of a nearly straight-edged crystal, which was grown under conditions of a 10:1 WO_3:NaCl ratio, reveal emission whose wavelength and bandwidth are spatially uniform across the crystal (Figure 5a, Figure S12). However, crystals prepared at 8:1 and 4:1 WO_3:NaCl ratios (higher W flux) exhibit an increased disorder in their PL characteristics (Figure 5b,c). PL maps of crystals grown at a 4:1 ratio identify significant variations in emission wavelength, intensity, and bandwidth across the crystal (Figure 5c).

Parametric plots of emission peak wavelength, intensity, and bandwidth summarize the progression toward increased optical disorder as morphological disorder increases in crystals grown at increasingly higher W flux (Figure 5a−c). As one progresses from crystals synthesized at 10:1 to 4:1 ratios, there is a marked increase in dispersion of the peak emission wavelength and an increase in the bandwidth of these emission peaks. Moreover, much of the emission broadening and site-to-site variation in the emission bandwidth appears localized to a region within ∼2 μm of the disordered edge of the crystal grown at a 4:1 ratio. Previous nano-optical characterization of 2D MoS_2 crystals identified a qualitatively similar dispersion in the emission energy and line-shape within energetically disordered regions located near the crystal edge.[26] A high density of edge protrusions, as in the case of WSe_2 growth at a 4:1 ratio, may cause increased lattice strain, as adjacent facets intersect. Lattice strain is known to alter overlap between atomic orbitals leading to shifted electronic bands, even when the strain field is localized to a few nanometers.[48,49] While in principle this strain could manifest as a Raman peak shift, we estimate from the observed 10−20 meV PL shifts that these crystals exhibit a modest lattice strain of less than 0.2%, which would render Raman peak shifts of less than 0.1 cm^{-1} that are less than the measurement limit of our instrument.[50,51]

Strain introduced by a rapid shift from equilibrium growth conditions is the most plausible explanation for the observed shifts in the energy of and disorder in PL. However, we also sought to address the possibility that chemical doping may be responsible for the observed spatial variations in PL, as has recently been shown in CVD-grown TMDs.[52] X-ray photoelectron spectroscopy (XPS) of salt-assisted 2D WSe_2 crystals grown on SiO_2 substrates shows no photoelectron signal from either Na 1s (expected at 1072 eV) or Cl 2p (expected at 198 eV) states (Figure S13). These data indicate that neither Na nor Cl is incorporated into the crystal lattice or adsorbed onto its surface after reaction. Moreover, these results are consistent with both our analysis of the precursor chemistry through XRD and with studies from the literature that discuss the proposed reaction pathway for NaCl-assisted growth of TMDs.[41,44] In these reactions, Na-containing species remain in the solid state and can be collected from the ceramic vessel, while volatile tungsten oxyhalide species, which are the primary WSe_2 precursor, react with H_2 to form H_2O and HCl byproducts, which remain in the gas phase to be expelled by the carrier gas.

https://doi.org/10.1021/acsnanoscienceau.3c00028
ACS Nanosci. Au 2023, 3, 441−450

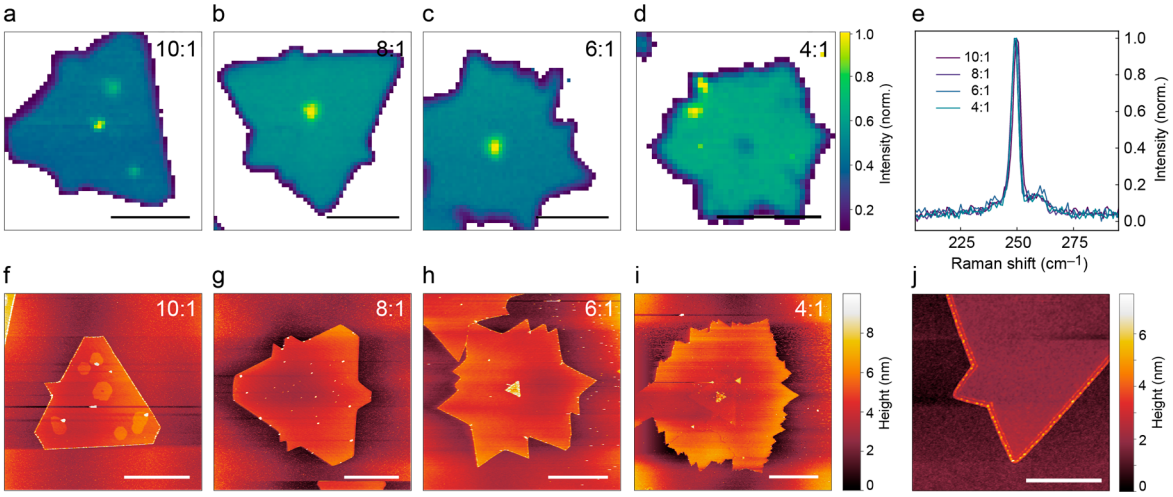

Figure 4. (a–d) Intensity-normalized Raman maps of integrated E′ peak intensity across a 2D WSe_2 crystal prepared at each of the ratios identified at top right. Scalebars: 10 μm. (e) Representative normalized Raman spectra for each mapped crystal identify a uniform E′ peak shift, line width, and profile. (f–i) AFM maps of crystals prepared at the listed ratios reveal the crystals to be of uniform height. Scalebars: 10 μm. (j) High-resolution AFM map of an edge protrusion. Scalebar: 2 μm.

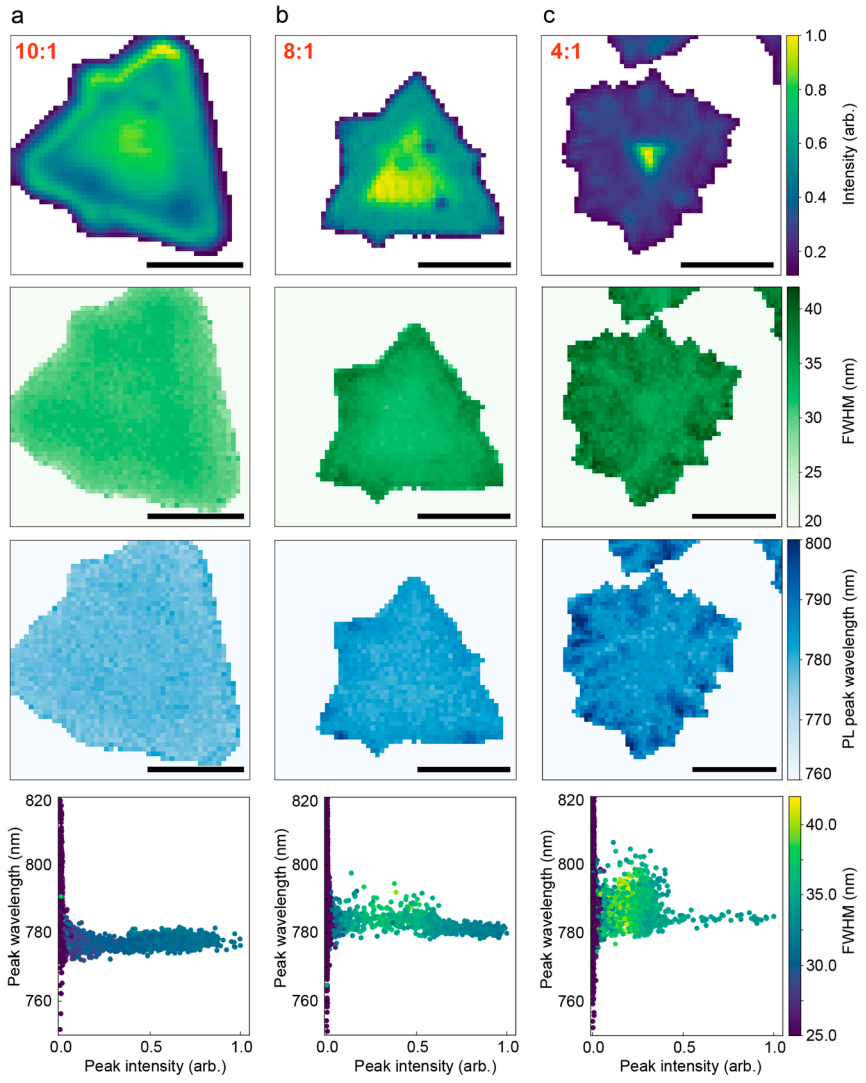

Figure 5. (a) From top to bottom, a map of normalized PL peak intensity, a map of PL peak bandwidth expressed as full-width at half-maximum (fwhm), a map of PL peak wavelength, and a parametric plot showing PL peak center wavelength, peak intensity, and peak fwhm for a WSe_2 crystal grown at a WO_3:NaCl ratio of (a) 10:1, (b) 8:1, and (c) 4:1. Scalebars: 10 μm.

https://doi.org/10.1021/acsnanoscienceau.3c00028
ACS Nanosci. Au 2023, 3, 441–450

We propose that future experiments should address the nature of the precursor chemistry during the reaction, for instance through the use of in situ methods such as mass spectrometry or ex-situ EDS analysis of under-reacted crystals. Therefore, we propose that structural disorder introduced under high W flux conditions leads to residual lattice strain that in turn shifts the exciton or charged exciton populations to yield the disordered emission profile near the edge of the jagged crystals. Further studies, for instance on suspended or transferred crystals, will shed additional light on the nature of synthetically induced strain.

CONCLUSION

In this study, we demonstrated that the transition metal precursor flux has a profound effect on the morphology and optical properties of 2D TMD crystals. We demonstrated systematic control over W precursor volatility, and thereby flux, by tuning the mass ratio of WO_3:NaCl mixtures, and we note that salt-assisted approaches may beneficially reduce the need for additional reducing agents during synthesis of TMDs. We explain the steady evolution of the crystal morphology and identify the emergence of a disordered growth mode at high W flux that yields WSe_2 crystals with jagged edges. These jagged edges are composed of oriented facet protrusions that nucleate around the circumference of the crystal due to an imbalance between the W_{zz} and Se_{zz} facet growth kinetics. Though morphologically disordered at its edges, the crystal still retains its continuous monolayer character with no evidence of apparent intergrowths. PL mapping shows that broadened and spatially varying emission profiles, most likely resulting from excitonic disorder, correlate strongly with the degree of structural disorder in the crystal. Studies correlating synthetic parameters, material morphology, and optoelectronic properties are vital for advancing a unified understanding of limits and opportunities in synthetic 2D materials.

METHODS

Chemical Analysis of WO_3:NaCl Precursors

Thermogravimetric analysis (TGA) of WO_3:NaCl mixtures in ratios of 5:1, 10:1, and 15:1 was conducted with a PerkinElmer TGA 8000. The samples were measured under a nitrogen atmosphere with a N_2 flow rate of 20 mL/min while being heated from room temperature to 900 °C at a rate of 32 °C/min.

Powder X-ray diffraction (pXRD) data were collected on samples composed of mixtures of WO_3 and NaCl (at the stated ratios) that were annealed in an alumina crucible in the presence of a hydrogen and selenium atmosphere identical with that used in the CVD reactions. Room-temperature pXRD scans were collected on these powder samples on a Bruker D8 Focus diffractometer (Cu source Kα = 8.04 keV, 1.5406 Å). Scans were taken over a 5−60° range with a 0.018585749° step size over 4 min.

Chemical Vapor Deposition Growth of WSe_2

CVD growth of WSe_2 was conducted in a custom-built CVD reactor, the details of which have been described previously.[16] Briefly, a quartz tube was cleaned with alconox, rinsed with water and IPA, dried under a N_2 flow, and baked out at 500 °C for 30 min. WO_3 (99.8% metals basis, Alfa Aesar) and NaCl (99.0%, EMD) were then mixed at mass ratios between 45:1 and 4:1, while keeping the NaCl mass constant at 3.5 mg, and spread evenly over the bottom of an alumina boat. A SiO_2 on Si substrate (SiO_2 layer is 200 nm thick) was then placed face-down on the alumina boat so as to cover the WO_3:NaCl powder. This substrate−boat ensemble was placed in the most downstream zone of our 3-zone furnace. A second alumina boat containing 200 mg of Se (99.5% metals basis, Alfa Aesar) was placed in the most upstream zone. The quartz tube was then evacuated to base pressure (~1×10^{-4} Torr) and pressurized to 5 Torr with 5 sccm of H_2 gas. The reactor was then heated to 850 °C over the course of 25 min and held at 850 °C for 3 min. After 3 min, the reaction was quenched by turning off the heating program and by flushing the reactor with 50 sccm of N_2 at 5 Torr. The furnace was cooled to room temperature.

Physical Characterization of WSe_2 Crystals

Crystals were imaged with an optical microscope (Zeiss Axioscope A1), a scanning electron microscope (Tescan Mira), and an aberration-corrected scanning transmission electron microscope (Nion UltraSTEM200X). SEM images were collected through an in-lens detector at an acceleration voltage of 10 kV, a beam current of 102 μA, and a working distance of 4 mm. Samples for STEM imaging were prepared by transferring 2D WSe_2 crystals with a polydimethylsiloxane (PDMS) stamp to a perforated SiN_x membrane TEM grid. Briefly, a PDMS stamp is placed on the desired region of the growth substrate; this stack is then immersed in a 1 M KOH solution until the stamp delaminates with the crystals. Using a microscope slide to support the stamp and a home-built transfer stage, the crystals are stamped and released onto perforated areas of the SiN_x membrane TEM grid. STEM images were collected by using high-angle annular dark field (HAADF) detection at an operating voltage of 60 kV with a nominal probe current and size of 30 pA and 120 pm, respectively. Optical and SEM images were analyzed with ImageJ to extract crystal sizes; edge protrusions were counted manually, and STEM-HAADF data were processed using Gatan DigitalMicrograph v3 for Fourier-filtering of images.

PL spectra shown in Figure 4 were taken with a Horiba Jobin Yvon T46000 spectrometer and a liquid N_2-cooled CCD detector. Excitation with an Ar^+/Kr^+ laser at 514 nm and 1 mW was focused through a 100x objective (Olympus) to a spot size of less than 1 μm. Raman and PL mapping was conducted on a LabRam Aramis (Horiba) system equipped with a Synapse spectrometer. Laser excitation at λ = 532 nm and a power of 1 mW was provided with a solid state laser focused through a 100× objective (Olympus) to a spot size of less than 1 μm. Raman and PL data were analyzed with Python, and an example of the data analyses performed can be found in Figure S11.

AFM maps were acquired on an MFP-3D (Asylum) AFM instrument operating in tapping mode with Si tips. AFM data were analyzed with Gwyddion.

ASSOCIATED CONTENT

Supporting Information

The Supporting Information is available free of charge at https://pubs.acs.org/doi/10.1021/acsnanoscienceau.3c00028.

(i) pXRD data of precursor, (ii) SEM and optical images of WSe_2 crystals, (iii) statistical analyses, (iv) TEM data, (v) Raman spectra, (vi) AFM scans, (vii) photoluminescence spectra, and (viii) XPS data (PDF)

AUTHOR INFORMATION

Corresponding Author

Thomas J. Kempa − *Department of Chemistry, Johns Hopkins University, Baltimore, Maryland 21218, United States of America; Department of Materials Science and Engineering, Johns Hopkins University, Baltimore, Maryland 21218, United States of America;* orcid.org/0000-0002-1672-8325; Email: tkempa@jhu.edu

Authors

Reynolds Dziobek-Garrett − *Department of Chemistry, Johns Hopkins University, Baltimore, Maryland 21218, United States of America;* orcid.org/0000-0002-8378-1230

https://doi.org/10.1021/acsnanoscienceau.3c00028
ACS Nanosci. Au 2023, 3, 441−450

Sachi Hilliard − *Department of Chemistry, Johns Hopkins University, Baltimore, Maryland 21218, United States of America;* orcid.org/0009-0000-2166-5739
Shreya Sriramineni − *Department of Chemistry, Johns Hopkins University, Baltimore, Maryland 21218, United States of America*
Ona Ambrozaite − *Department of Chemistry, Johns Hopkins University, Baltimore, Maryland 21218, United States of America;* orcid.org/0000-0003-1464-2111
Yifei Zhu − *Department of Chemistry, Johns Hopkins University, Baltimore, Maryland 21218, United States of America*
Bethany M. Hudak − *Materials Science & Technology Division, U.S. Naval Research Laboratory, Washington, D.C. 20375, United States of America;* orcid.org/0000-0002-4392-9237
Todd H. Brintlinger − *Materials Science & Technology Division, U.S. Naval Research Laboratory, Washington, D.C. 20375, United States of America*
Tomojit Chowdhury − *Department of Chemistry and Chicago Materials Research Center, University of Chicago, Chicago, Illinois 60637, United States of America;* orcid.org/0000-0002-6841-0642

Complete contact information is available at: https://pubs.acs.org/10.1021/acsnanoscienceau.3c00028

Author Contributions

R.D.G. and T.J.K. conceived the study and designed experiments. R.D.G. and T.C. performed initial syntheses. R.D.G. performed subsequent syntheses with assistance from S.H. and O.A. Y.Z. collected pXRD data. R.D.G. performed structural and optical characterization of crystals. R.D.G., T.H.B., and B.H. prepared samples and collected scanning transmission electron microscopy data. S.S. performed image analysis. R.D.G., T.C., and T.J.K. wrote the manuscript with input from all authors. All authors have given approval to the final version of the manuscript. CRediT: **Reynolds Dziobek-Garrett** conceptualization (equal), data curation (equal), formal analysis (equal), investigation (equal), validation (equal), visualization (equal), writing-original draft (equal), writing-review & editing (equal); **Sachi Hilliard** investigation (equal), validation (equal); **Shreya Sriramineni** investigation (equal), software (equal); **Ona Ambrozaite** investigation (equal), validation (equal); **Yifei Zhu** investigation (equal), validation (equal); **Bethany M. Hudak** formal analysis (equal), investigation (equal); **Todd H. Brintlinger** formal analysis (equal), investigation (equal); **Tomojit Chowdhury** investigation (equal), methodology (equal); **Thomas J Kempa** conceptualization (equal), data curation (equal), formal analysis (equal), funding acquisition (lead), methodology (lead), project administration (lead), resources (lead), software (equal), supervision (lead), visualization (equal), writing-original draft (equal), writing-review & editing (lead).

Funding

T.J.K. acknowledges funding from a National Science Foundation (DMR-1848046) CAREER grant which supported characterization studies in this work. T.J.K. also acknowledges funding for this study by the Young Faculty Award program of the Defense Advanced Research Projects Agency (DARPA) and by the Army Research Office under the grant W911NF-21-1-0351. T.H.B. and B.H. were supported by the Office of Naval Research through the U.S. Naval Research Laboratory base program. The views, opinions, and/or findings expressed are those of the authors and should not be interpreted as representing the official views or policies of the Department of Defense or the U.S. Government.

Notes

The authors declare no competing financial interest.

■ ABBREVIATIONS

TMD, transition metal dichalcogenide; CVD, chemical vapor deposition; PL, photoluminescence; OM, optical microscopy; SEM, scanning electron microscopy; AFM, atomic force microscopy; TGA, thermogravimetric analysis; pXRD, powder X-ray diffraction

■ REFERENCES

(1) Ross, J. S.; Klement, P.; Jones, A. M.; Ghimire, N. J.; Yan, J.; Mandrus, D. G.; Taniguchi, T.; Watanabe, K.; Kitamura, K.; Yao, W.; Cobden, D. H.; Xu, X. Electrically Tunable Excitonic Light-Emitting Diodes Based on Monolayer WSe2 p-n Junctions. *Nat. Nanotechnol* **2014**, *9* (4), 268−272.
(2) Withers, F.; Del Pozo-Zamudio, O.; Mishchenko, A.; Rooney, A. P.; Gholinia, A.; Watanabe, K.; Taniguchi, T.; Haigh, S. J.; Geim, A. K.; Tartakovskii, A. I.; Novoselov, K. S. Light-Emitting Diodes by Band-Structure Engineering in van Der Waals Heterostructures. *Nat. Mater.* **2015**, *14* (3), 301−306.
(3) Mak, K. F.; Shan, J. Photonics and Optoelectronics of 2D Semiconductor Transition Metal Dichalcogenides. *Nat. Photonics* **2016**, *10* (4), 216−226.
(4) Radisavljevic, B.; Radenovic, A.; Brivio, J.; Giacometti, V.; Kis, A. Single-Layer MoS2 Transistors. *Nat. Nanotechnol* **2011**, *6* (3), 147−150.
(5) Desai, S. B.; Madhvapathy, S. R.; Sachid, A. B.; Llinas, J. P.; Wang, Q.; Ahn, G. H.; Pitner, G.; Kim, M. J.; Bokor, J.; Hu, C.; Wong, H. S. P.; Javey, A. MoS2 Transistors with 1-Nanometer Gate Lengths. *Science (1979)* **2016**, *354* (6308), 99−102.
(6) Wang, K.; De Greve, K.; Jauregui, L. A.; Sushko, A.; High, A.; Zhou, Y.; Scuri, G.; Taniguchi, T.; Watanabe, K.; Lukin, M. D.; Park, H.; Kim, P. Electrical Control of Charged Carriers and Excitons in Atomically Thin Materials. *Nat. Nanotechnol* **2018**, *13* (2), 128−132.
(7) Palacios-Berraquero, C.; Barbone, M.; Kara, D. M.; Chen, X.; Goykhman, I.; Yoon, D.; Ott, A. K.; Beitner, J.; Watanabe, K.; Taniguchi, T.; Ferrari, A. C.; Atatüre, M. Atomically Thin Quantum Light-Emitting Diodes. *Nat. Commun.* **2016**, *7*, 1−6.
(8) Ciarrocchi, A.; Tagarelli, F.; Avsar, A.; Kis, A. Excitonic Devices with van Der Waals Heterostructures: Valleytronics Meets Twistronics. *Nat. Rev. Mater.* **2022**, *7* (6), 449−464.
(9) Zeng, H.; Cui, X. An Optical Spectroscopic Study on Two-Dimensional Group-VI Transition Metal Dichalcogenides. *Chem. Soc. Rev.* **2015**, *44* (9), 2629−2642.
(10) Mak, K. F.; Lee, C.; Hone, J.; Shan, J.; Heinz, T. F. Atomically Thin MoS2: A New Direct-Gap Semiconductor. *Phys. Rev. Lett.* **2010**, *105* (13), 6805.
(11) Chernikov, A.; Berkelbach, T. C.; Hill, H. M.; Rigosi, A.; Li, Y.; Aslan, O. B.; Reichman, D. R.; Hybertsen, M. S.; Heinz, T. F. Exciton Binding Energy and Nonhydrogenic Rydberg Series in Monolayer WS2. *Phys. Rev. Lett.* **2014**, *113* (7), 1−5.
(12) Mak, K. F.; He, K.; Shan, J.; Heinz, T. F. Control of Valley Polarization in Monolayer MoS2 by Optical Helicity. *Nat. Nanotechnol* **2012**, *7* (8), 494−498.
(13) Geim, A. K.; Grigorieva, I. v. Van Der Waals Heterostructures. *Nature* **2013**, *499* (7459), 419−425.
(14) Chen, P.; Zhang, Z.; Duan, X.; Duan, X. Chemical Synthesis of Two-Dimensional Atomic Crystals, Heterostructures and Superlattices. *Chem. Soc. Rev.* **2018**, *47* (9), 3129−3151.
(15) Lin, Y. C.; Yeh, C. H.; Lin, H. C.; Siao, M. D.; Liu, Z.; Nakajima, H.; Okazaki, T.; Chou, M. Y.; Suenaga, K.; Chiu, P. W.

Stable 1T Tungsten Disulfide Monolayer and Its Junctions: Growth and Atomic Structures. *ACS Nano* **2018**, *12* (12), 12080−12088.
(16) Chowdhury, T.; Kim, J.; Sadler, E. C.; Li, C.; Lee, S. W.; Jo, K.; Xu, W.; Gracias, D. H.; Drichko, N. v.; Jariwala, D.; Brintlinger, T. H.; Mueller, T.; Park, H. G.; Kempa, T. J. Substrate-Directed Synthesis of MoS2 Nanocrystals with Tunable Dimensionality and Optical Properties. *Nat. Nanotechnol* **2020**, *15* (1), 29−34.
(17) Aljarb, A.; Fu, J. H.; Hsu, C. C.; Chuu, C. P.; Wan, Y.; Hakami, M.; Naphade, D. R.; Yengel, E.; Lee, C. J.; Brems, S.; Chen, T. A.; Li, M. Y.; Bae, S. H.; Hsu, W. T.; Cao, Z.; Albaridy, R.; Lopatin, S.; Chang, W. H.; Anthopoulos, T. D.; Kim, J.; Li, L. J.; Tung, V. Ledge-Directed Epitaxy of Continuously Self-Aligned Single-Crystalline Nanoribbons of Transition Metal Dichalcogenides. *Nat. Mater.* **2020**, *19* (9), 1300−1306.
(18) Najmaei, S.; Liu, Z.; Zhou, W.; Zou, X.; Shi, G.; Lei, S.; Yakobson, B. I.; Idrobo, J. C.; Ajayan, P. M.; Lou, J. Vapour Phase Growth and Grain Boundary Structure of Molybdenum Disulphide Atomic Layers. *Nat. Mater.* **2013**, *12* (8), 754−759.
(19) Van Der Zande, A. M.; Huang, P. Y.; Chenet, D. A.; Berkelbach, T. C.; You, Y.; Lee, G. H.; Heinz, T. F.; Reichman, D. R.; Muller, D. A.; Hone, J. C. Grains and Grain Boundaries in Highly Crystalline Monolayer Molybdenum Disulphide. *Nat. Mater.* **2013**, *12* (6), 554−561.
(20) Kim, H.; Ahn, G. H.; Cho, J.; Amani, M.; Mastandrea, J. P.; Groschner, C. K.; Lien, D. H.; Zhao, Y.; Ager, J. W.; Scott, M. C.; Chrzan, D. C.; Javey, A. Synthetic WSe 2 Monolayers with High Photoluminescence Quantum Yield. *Sci. Adv.* **2019**, *5*, eaau4728.
(21) Rhodes, D.; Chae, S. H.; Ribeiro-Palau, R.; Hone, J. Disorder in van Der Waals Heterostructures of 2D Materials. *Nat. Mater.* **2019**, *18* (6), 541−549.
(22) Liu, Z.; Amani, M.; Najmaei, S.; Xu, Q.; Zou, X.; Zhou, W.; Yu, T.; Qiu, C.; Birdwell, A. G.; Crowne, F. J.; Vajtai, R.; Yakobson, B. I.; Xia, Z.; Dubey, M.; Ajayan, P. M.; Lou, J. Strain and Structure Heterogeneity in MoS 2 Atomic Layers Grown by Chemical Vapour Deposition. *Nat. Commun.* **2014**, *5*, 6246.
(23) Ahn, G. H.; Amani, M.; Rasool, H.; Lien, D. H.; Mastandrea, J. P.; Ager, J. W.; Dubey, M.; Chrzan, D. C.; Minor, A. M.; Javey, A. Strain-Engineered Growth of Two-Dimensional Materials. *Nat. Commun.* **2017**, *8*, 608.
(24) Jaramillo, T. F.; Jørgensen, K. P.; Bonde, J.; Nielsen, J. H.; Horch, S.; Chorkendorff, I. Identification of Active Edge Sites for Electrochemical H2 Evolution from MoS2 Nanocatalysts. *Science (1979)* **2007**, *317* (5834), 100−102.
(25) Kim, M. S.; Yun, S. J.; Lee, Y.; Seo, C.; Han, G. H.; Kim, K. K.; Lee, Y. H.; Kim, J. Biexciton Emission from Edges and Grain Boundaries of Triangular WS2Monolayers. *ACS Nano* **2016**, *10* (2), 2399−2405.
(26) Bao, W.; Borys, N. J.; Ko, C.; Suh, J.; Fan, W.; Thron, A.; Zhang, Y.; Buyanin, A.; Zhang, J.; Cabrini, S.; Ashby, P. D.; Weber-Bargioni, A.; Tongay, S.; Aloni, S.; Ogletree, D. F.; Wu, J.; Salmeron, M. B.; Schuck, P. J. Visualizing Nanoscale Excitonic Relaxation Properties of Disordered Edges and Grain Boundaries in Monolayer Molybdenum Disulfide. *Nat. Commun.* **2015**, *6*, 7993.
(27) Liu, L.; Ge, Z.; Yan, C.; Moghadam, A. D.; Weinert, M.; Li, L. Termination-Dependent Edge States of MBE-Grown WSe2. *Phys. Rev. B* **2018**, *98* (23), 235304.
(28) Addou, R.; Smyth, C. M.; Noh, J. Y.; Lin, Y. C.; Pan, Y.; Eichfeld, S. M.; Fölsch, S.; Robinson, J. A.; Cho, K.; Feenstra, R. M.; Wallace, R. M. One Dimensional Metallic Edges in Atomically Thin WSe2 Induced by Air Exposure. *2d Mater.* **2018**, *5* (2), 025017.
(29) Tao, L.; Meng, F.; Zhao, S.; Song, Y.; Yu, J.; Wang, X.; Liu, Z.; Wang, Y.; Li, B.; Wang, Y.; Sui, Y. Experimental and Theoretical Evidence for the Ferromagnetic Edge in WSe2 Nanosheets. *Nanoscale* **2017**, *9* (15), 4898−4906.
(30) Ugeda, M. M.; Pulkin, A.; Tang, S.; Ryu, H.; Wu, Q.; Zhang, Y.; Wong, D.; Pedramrazi, Z.; Martín-Recio, A.; Chen, Y.; Wang, F.; Shen, Z. X.; Mo, S. K.; Yazyev, O. V.; Crommie, M. F. Observation of Topologically Protected States at Crystalline Phase Boundaries in Single-Layer WSe2. *Nature Communications 2018 9:1* **2018**, *9* (1), 1−7.
(31) Xu, J.; Ho, D. Modulation of the Reaction Mechanism via S/Mo: A Rational Strategy for Large-Area MoS2Growth. *Chem. Mater.* **2021**, *33* (9), 3249−3257.
(32) Kim, I. S.; Sangwan, V. K.; Jariwala, D.; Wood, J. D.; Park, S.; Chen, K. S.; Shi, F.; Ruiz-Zepeda, F.; Ponce, A.; Jose-Yacaman, M.; Dravid, V. P.; Marks, T. J.; Hersam, M. C.; Lauhon, L. J. Influence of Stoichiometry on the Optical and Electrical Properties of Chemical Vapor Deposition Derived MoS2. *ACS Nano* **2014**, *8* (10), 10551−10558.
(33) Liu, B.; Fathi, M.; Chen, L.; Abbas, A.; Ma, Y.; Zhou, C. Chemical Vapor Deposition Growth of Monolayer WSe2 with Tunable Device Characteristics and Growth Mechanism Study. *ACS Nano* **2015**, *9* (6), 6119−6127.
(34) Wang, S.; Rong, Y.; Fan, Y.; Pacios, M.; Bhaskaran, H.; He, K.; Warner, J. H. Shape Evolution of Monolayer MoS2 Crystals Grown by Chemical Vapor Deposition. *Chem. Mater.* **2014**, *26* (22), 6371−6379.
(35) Cao, D.; Shen, T.; Liang, P.; Chen, X.; Shu, H. Role of Chemical Potential in Flake Shape and Edge Properties of Monolayer MoS2. *J. Phys. Chem. C* **2015**, *119* (8), 4294−4301.
(36) Li, X.; Zhang, S.; Chen, S.; Zhang, X.; Gao, J.; Zhang, Y.-W.; Zhao, J.; Shen, X.; Yu, R.; Yang, Y.; He, L.; Nie, J.; Xiong, C.; Dou, R. Mo Concentration Controls the Morphological Transitions from Dendritic to Semicompact, and to Compact Growth of Monolayer Crystalline MoS2 on Various Substrates. *ACS Appl. Mater. Interfaces* **2019**, *11* (45), 42751−42759.
(37) Xu, J.; Srolovitz, D. J.; Ho, D. The Adatom Concentration Profile: A Paradigm for Understanding Two-Dimensional MoS 2 Morphological Evolution in Chemical Vapor Deposition Growth. *ACS Nano* **2021**, *15* (4), 6839−6848.
(38) Govind Rajan, A.; Warner, J. H.; Blankschtein, D.; Strano, M. S. Generalized Mechanistic Model for the Chemical Vapor Deposition of 2D Transition Metal Dichalcogenide Monolayers. *ACS Nano* **2016**, *10* (4), 4330−4344.
(39) Lee, Y.; Jeong, H.; Park, Y. S.; Han, S.; Noh, J.; Lee, J. S. Anisotropic Growth Mechanism of Tungsten Diselenide Domains Using Chemical Vapor Deposition Method. *Appl. Surf. Sci.* **2018**, *432*, 170−175.
(40) Li, S.; Wang, S.; Tang, D. M.; Zhao, W.; Xu, H.; Chu, L.; Bando, Y.; Golberg, D.; Eda, G. Halide-Assisted Atmospheric Pressure Growth of Large WSe2 and WS2Monolayer Crystals. *Appl. Mater. Today* **2015**, *1* (1), 60−66.
(41) Zhou, J.; Lin, J.; Huang, X.; Zhou, Y.; Chen, Y.; Xia, J.; Wang, H.; Xie, Y.; Yu, H.; Lei, J.; Wu, D.; Liu, F.; Fu, Q.; Zeng, Q.; Hsu, C. H.; Yang, C.; Lu, L.; Yu, T.; Shen, Z.; Lin, H.; Yakobson, B. I.; Liu, Q.; Suenaga, K.; Liu, G.; Liu, Z. A Library of Atomically Thin Metal Chalcogenides. *Nature* **2018**, *556* (7701), 355−359.
(42) Diehl, R.; Brandt, G. The Crystal Structure of Triclinic WO3. *Acta Crystallogr.* **1978**, *B34*, 1105−1111.
(43) Straumanis, M. E. Chemical Properties and Structure. *J. Am. Chem. Soc.* **1949**, *71* (2), 679−683.
(44) Lei, J.; Xie, Y.; Kutana, A.; Bets, K. V.; Yakobson, B. I. Salt-Assisted MoS2 Growth: Molecular Mechanisms from the First Principles. *J. Am. Chem. Soc.* **2022**, *144* (16), 7497−7503.
(45) Yoo, Y.; Degregorio, Z. P.; Johns, J. E. Seed Crystal Homogeneity Controls Lateral and Vertical Heteroepitaxy of Monolayer MoS2 and WS2. *J. Am. Chem. Soc.* **2015**, *137* (45), 14281−14287.
(46) Cain, J. D.; Shi, F.; Wu, J.; Dravid, V. P. Growth Mechanism of Transition Metal Dichalcogenide Monolayers: The Role of Self-Seeding Fullerene Nuclei. *ACS Nano* **2016**, *10* (5), 5440−5445.
(47) Sadler, E. C.; Kempa, T. J. Chalcogen Incorporation Process during High-Vacuum Conversion of Bulk Mo Oxides to Mo Dichalcogenides. *ACS Appl. Electron Mater.* **2020**, *2* (4), 1020−1025.
(48) Schmidt, R.; Niehues, I.; Schneider, R.; Druppel, M.; Deilmann, T.; Rohlfing, M.; de Vasconcellos, S. M.; Castellanos-Gomez, A.;

Bratschitsch, R. Reversible Uniaxial Strain Tuning in Atomically Thin WSe2. *2d Mater.* **2016**, *3* (2), 021011.
(49) Chowdhury, T.; Jo, K.; Anantharaman, S. B.; Brintlinger, T. H.; Jariwala, D.; Kempa, T. J. Anomalous Room-Temperature Photoluminescence from Nanostrained MoSe2Monolayers. *ACS Photonics* **2021**, *8* (8), 2220−2226.
(50) He, K.; Poole, C.; Mak, K. F.; Shan, J. Experimental Demonstration of Continuous Electronic Structure Tuning via Strain in Atomically Thin MoS2. *Nano Lett.* **2013**, *13* (6), 2931−2936.
(51) Dadgar, A. M.; Scullion, D.; Kang, K.; Esposito, D.; Yang, E. H.; Herman, I. P.; Pimenta, M. A.; Santos, E. J. G.; Pasupathy, A. N. Strain Engineering and Raman Spectroscopy of Monolayer Transition Metal Dichalcogenides. *Chem. Mater.* **2018**, *30* (15), 5148−5155.
(52) Zhang, T.; Liu, M.; Fujisawa, K.; Lucking, M.; Beach, K.; Zhang, F.; Shanmugasundaram, M.; Krayev, A.; Murray, W.; Lei, Y.; Yu, Z.; Sanchez, D.; Liu, Z.; Terrones, H.; Elías, A. L.; Terrones, M. Spatial Control of Substitutional Dopants in Hexagonal Monolayer WS2: The Effect of Edge Termination. *Small* **2023**, *19* (6), 2205800.

https://doi.org/10.1021/acsnanoscienceau.3c00028
ACS Nanosci. Au 2023, 3, 441−450